Turbulence Modeling in Three-Dimensional Stenosed Arterial Bifurcations

J. Banks
e-mail: jb17@soton.ac.uk

N. W. Bressloff[1]
e-mail: N.W.Bressloff@soton.ac.uk

Computational Engineering and Design Group,
University of Southampton,
Highfield, Southampton SO17 1BJ, U.K.

Under normal healthy conditions, blood flow in the carotid artery bifurcation is laminar. However, in the presence of a stenosis, the flow can become turbulent at the higher Reynolds numbers during systole. There is growing consensus that the transitional $k-\omega$ model is the best suited Reynolds averaged turbulence model for such flows. Further confirmation of this opinion is presented here by a comparison with the RNG $k-\epsilon$ model for the flow through a straight, nonbifurcating tube. Unlike similar validation studies elsewhere, no assumptions are made about the inlet profile since the full length of the experimental tube is simulated. Additionally, variations in the inflow turbulence quantities are shown to have no noticeable affect on downstream turbulence intensity, turbulent viscosity, or velocity in the $k-\epsilon$ model, whereas the velocity profiles in the transitional $k-\omega$ model show some differences due to large variations in the downstream turbulence quantities. Following this validation study, the transitional $k-\omega$ model is applied in a three-dimensional parametrically defined computer model of the carotid artery bifurcation in which the sinus bulb is manipulated to produce mild, moderate, and severe stenosis. The parametric geometry definition facilitates a powerful means for investigating the effect of local shape variation while keeping the global shape fixed. While turbulence levels are generally low in all cases considered, the mild stenosis model produces higher levels of turbulent viscosity and this is linked to relatively high values of turbulent kinetic energy and low values of the specific dissipation rate. The severe stenosis model displays stronger recirculation in the flow field with higher values of vorticity, helicity, and negative wall shear stress. The mild and moderate stenosis configurations produce similar lower levels of vorticity and helicity. [DOI: 10.1115/1.2401182]

1 Introduction

Parametrically defined computer aided design (CAD) enables the manipulation of the local shape of a geometry while keeping the global shape constant. This feature of CAD is exploited here to generate mild, moderate, and severely stenosed sinus bulbs (in an average carotid artery bifurcation) so as to investigate how variations in levels of turbulence, produced by local narrowing of the artery, affect the overall flow field. Such an approach is attractive since its focus on the interaction between shape and turbulence should enhance our understanding of the haemodynamics in stenosed arteries.

Disease within the cardio-vascular system is responsible for millions of deaths worldwide [1]. Specific arteries are prone to disease initiation and various effects are responsible for damage to these arteries: biochemical, haemodynamic, and geometric. Arteries with curvature or bifurcation regions are particularly vulnerable to the initiation of cardio-vascular diseases [2,3]. Pulsatile flow conditions occur within the cardio-vascular system with significant differences between systole and diastole. Typical Reynolds numbers for blood flow within the arterial tree range from 1 to 4000 [2]. Although laminar flow conditions exist for the majority of arteries throughout the cardiovascular system, large accelerations through bifurcation regions during systole where a reduction in the diameter of the artery is present can lead to turbulence being generated.

The carotid artery bifurcation, where the common carotid artery splits into the internal carotid and external carotid artery, is particularly prone to the initiation and buildup of atherosclerosis. The initiation of disease is strongly correlated to the geometric shape of the bifurcation, in particular the sinus bulb at the base of the internal carotid artery (ICA). A characteristic buildup of fatty deposits within the internal carotid sinus bulb is observed that leads to a narrowing of the artery. It is the presence of the stenosis that can cause the flow within arteries to change from normal laminar conditions to turbulent flow. The wide variation in the dimensions of the carotid artery bifurcation is also believed to have an effect on the initiation of atherosclerosis and other cardio-vascular diseases [4].

One of the difficulties associated with modeling turbulent flow in computational fluid dynamics (CFD) concerns the selection of the most suitable turbulence model. Each model has its own strengths and weaknesses with some being designed purely for one type of flow regime. The problem of choosing which turbulence model to use is compounded by the many variations that may appear for each model. These variations usually try to address a problem with the original turbulence model to help achieve better results for particular test cases or to provide a more robust numerical scheme.

The $k-\omega$ turbulence model is currently favored for turbulent flow CFD simulations within arteries. This model seems to perform better than other turbulence models when compared against experimental data [5]. Stroud et al. [6] studied the Goldberg and Chien variants of the $k-\epsilon$ model within a two-dimensional (2D) severely stenosed model of the carotid artery bifurcation with the Chien variant performing better overall. All $k-\epsilon$ turbulence models use wall functions to obtain near-wall results. This is the region of particular interest in most arterial flows with respect to the initiation and buildup of disease. Therefore the $k-\epsilon$ family of turbulence models may not be the best option for blood flow problems. The $k-\omega$ model has provided some good comparisons to experimental data [7] and additional corrections can be applied for

[1]Corresponding author.

Contributed by the Bioengineering Division of ASME for publication in the JOURNAL OF BIOMECHANICAL ENGINEERING. Manuscript received May 25, 2005; final manuscript received July 28, 2006. Review conducted by David A. Steinman.

low Reynolds number transitional flows. The $k-\omega$ model also performs well close to the wall for boundary layer flows without using wall functions. Recent successful comparisons for flow in a smooth circular tube have also been reported for the $q-\zeta$ model [8].

A study analyzing large eddy simulation (LES) [9] used a simple stenosed channel geometry and a parabolic inflow velocity profile. The results suggest the flow downstream of the stenosis is transitional in nature and demonstrates LES may be well suited for use in arterial flow problems. Currently one of the problems with LES is the large computational cost required to perform relatively simple geometry studies; this study required approximately 500 CPU h. A further combined LES/direct numerical simulation (DNS) study [10] considers a range of Reynolds number using the simple stenosed channel geometry. For Reynolds number higher than 1000 the flow transitions to turbulence downstream of the stenosis.

No single turbulence model is able to provide the correct behavior for all of the wide range of flows modeled by CFD users. The use of DNS for flow simulations is currently in its infancy. Very few DNS studies have been undertaken at a valid Reynolds number because the computational cost and complexity of DNS excludes these real world flows from being fully modeled. DNS studies resolve every detail of the flow being modeled, hence the high computational cost. Currently the majority of DNS simulations are limited to low Reynolds number flows with very simple geometries. Even with these simple configurations such simulations typically take hundreds of hours to run [10].

Experimental work by Ahmed and Giddens [11] considered pulsatile flow through three plexiglass models with stenosis area reductions of 25%, 50%, and 75%. Profiles of the velocity were measured for each model and compared for various time locations. Flow visualisation was achieved by releasing hydrogen bubbles in the flow. Turbulent flow was only found in the 75% stenosis model and was present for a segment of the inflow cycle when the flow was decelerating. The turbulent flow was found to occur approximately 6 diameters downstream of the stenosis throat.

While the main focus here concerns the interaction between stenosis shape and turbulence, a preliminary study is presented that compares the renormalization group (RNG) variant of the $k-\epsilon$ model and the low Reynolds number (transitional flow) $k-\omega$ turbulence model against data obtained in experimental flow through a constricted tube from Ahmed and Giddens [11]. Simulations are then performed in the CAD generated models of the carotid artery bifurcation with various degrees of stenosis. The commercial CFD package FLUENT™v6.1.22 (Fluent, Inc.) was used for all simulations.

2 Turbulence Models

The flow simulations were setup using the RNG variant of the $k-\epsilon$ turbulence model and the low Reynolds number (transitional flow) version of the $k-\omega$ turbulence model. Preliminary work looked at a wide range of turbulence models available in the FLUENT package. Models that were tested but deemed unsuitable for arterial flows include the Spalart–Allmaras model, the $k-\omega$ shear stress transport (SST) model, the standard $k-\epsilon$ model, and the Reynolds stress model (RSM). Details of the formulation of the $k-\epsilon$ RNG and the low Reynolds number variant of $k-\omega$ within the FLUENT package are given in Sec. 2.1 and 2.2.

2.1 The $k-\epsilon$ RNG Model. The RNG variant of the $k-\epsilon$ model is derived from the Navier–Stokes equations using the (RNG) method. Using standard tensor notation, the equations have a form similar to the standard $k-\epsilon$ model, where, for turbulent kinetic energy k

Table 1 Model constants for $k-\epsilon$ RNG

C_μ	$C_{1\epsilon}$	$C_{2\epsilon}$
0.0845	1.42	1.68

$$\frac{\partial}{\partial t}(\rho k)+\frac{\partial}{\partial x_i}(\rho k u_i)=\frac{\partial}{\partial x_j}\left(\alpha_k \mu_{\text{eff}}\frac{\partial k}{\partial x_j}\right)+G_k-\rho\epsilon \tag{1}$$

and for the dissipation rate ϵ

$$\frac{\partial}{\partial t}(\rho\epsilon)+\frac{\partial}{\partial x_i}(\rho\epsilon u_i)=\frac{\partial}{\partial x_j}\left(\alpha_\epsilon \mu_{\text{eff}}\frac{\partial \epsilon}{\partial x_j}\right)+C_{1\epsilon}\frac{\epsilon}{k}G_k-C_{2\epsilon}\rho\frac{\epsilon^2}{k}-R_\epsilon \tag{2}$$

where the effective viscosity, μ_{eff}, is the sum of the molecular viscosity, μ, and the turbulent viscosity, μ_t.

The constants in Eqs. (9) and (2) are given in Table 1. The term G_k represents the generation of turbulence kinetic energy due to the mean velocity gradients and is defined as

$$G_k=-\rho\overline{u_i' u_j'}\frac{\partial u_j}{\partial x_i} \tag{3}$$

where fluctuating quantities are denoted by the (′) superscript.

Evaluating G_k using the Boussinesq hypothesis yields

$$G_k=\mu_t S^2 \tag{4}$$

as a function of the turbulent viscosity, μ_t, and S given by the modulus of the mean rate of strain tensor, defined as

$$S\equiv\sqrt{2S_{ij}S_{ij}} \tag{5}$$

The α_k and α_ϵ are the inverse Prandtl numbers for k and ϵ, respectively. The RNG version of the $k-\epsilon$ model introduces a new term into the ϵ transport equation, R_ϵ, and is defined as

$$R_\epsilon=\frac{C_\mu\rho\eta^3(1-\eta/\eta_0)}{1+\beta\eta^3}\frac{\epsilon}{k} \tag{6}$$

where $\eta\equiv Sk/\epsilon$, η_0=4.38, and β=0.012. The R_ϵ term improves the behavior of the model for rapidly strained flows such as that considered here.

The inverse Prandtl numbers for α_k and α_ϵ are calculated using the following relationship taken from RNG theory

$$\left|\frac{\alpha-1.3929}{\alpha_0-1.3929}\right|^{0.6321}\left|\frac{\alpha+2.3929}{\alpha_0+2.3929}\right|^{0.3679}=\frac{\mu}{\mu_{\text{eff}}} \tag{7}$$

with α_0=1. In the high Reynolds number limit ($\mu_{\text{mol}}/\mu_{\text{eff}}\ll 1$), $\alpha_k=\alpha_\epsilon$=1.393.

The effective viscosity, μ_{eff}, is calculated from the following differential equation

$$d\left(\frac{\rho^2 k}{\sqrt{\epsilon\mu}}\right)=1.72\frac{\hat{\nu}}{\sqrt{\hat{\nu}^3-1+C_\nu}}d\hat{\nu} \tag{8}$$

where $\hat{\nu}=\mu_{\text{eff}}/\mu$ and C_ν=100. At low Reynolds number the turbulent viscosity, μ_t, is obtained by integrating Eq. (8) while at high Reynolds numbers it equates to $\mu_t=\rho C_\mu(k/\epsilon)$.

2.2 Low Reynolds Number (Transitional) $k-\omega$ Model. In the $k-\omega$ model, the turbulent kinetic energy equation has a slightly different form 2 from the $k-\epsilon$ model given by

$$\frac{\partial}{\partial t}(\rho k)+\frac{\partial}{\partial x_i}(\rho k u_i)=\frac{\partial}{\partial x_j}\left(\Gamma_k\frac{\partial k}{\partial x_j}\right)+G_k-Y_k \tag{9}$$

Also, an equation for the specific dissipation rate, ω, is solved in place of ϵ and is formulated as

$$\frac{\partial}{\partial t}(\rho\omega)+\frac{\partial}{\partial x_i}(\rho\omega u_i)=\frac{\partial}{\partial x_j}\left(\Gamma_\omega\frac{\partial\omega}{\partial x_j}\right)+G_\omega-Y_\omega \tag{10}$$

Table 2 Model constants for the transitional $k-\omega$ model

α^*_∞	α_∞	α_0	β^*_∞	β_i	R_β	R_k	R_ω	ζ^*	M_{t0}	σ_k	σ_ω
1	0.52	0.11111	0.09	0.072	8	6	2.95	1.5	0.25	2	2

The constants for these two transport equations are given in Table 2. The term G_k denotes the generation of turbulent kinetic energy due to mean velocity gradients, and G_ω represents the generation of ω. Γ_k and Γ_ω signify the effective diffusivity of k and ω, respectively. The terms Y_k and Y_ω represent the dissipation of k and ω due to turbulence.

The effective diffusivities of k and ω are given by

$$\Gamma_k = \mu + \frac{\mu_t}{\sigma_k} \tag{11}$$

$$\Gamma_\omega = \mu + \frac{\mu_t}{\sigma_\omega} \tag{12}$$

where σ_k and σ_ω are the turbulent Prandtl numbers for k and ω, respectively. The turbulent viscosity, μ_t, is calculated using both k and ω

$$\mu_t = \alpha^* \frac{\rho k}{\omega} \tag{13}$$

where the coefficient α^* is a damping coefficient for the low Reynolds effects and is defined as

$$\alpha^* = \alpha^*_\infty \left(\frac{\alpha^*_0 + \mathrm{Re}_t/R_k}{1 + \mathrm{Re}_t/R_k} \right) \tag{14}$$

Both α^*_∞ and R_k are constants supplied to the turbulence model and have the values 1 and 6, respectively. The value for α^*_0 is calculated using another turbulence model coefficient, β_i $=0.072/3=0.024$ and Re_t is calculated using $\rho k/\mu\omega$.

The production of k is calculated using Eqs. (3)–(5) from the $k-\epsilon$ RNG model. The production of ω is calculated using

$$G_\omega = \alpha \frac{\omega}{k} G_k \tag{15}$$

using G_k as defined in Eq. (3). The coefficient α is given by

$$\alpha = \frac{\alpha_\infty}{\alpha^*} \left(\frac{\alpha_0 + \mathrm{Re}_t/R_\omega}{1 + \mathrm{Re}_t/R_\omega} \right) \tag{16}$$

where $R_\omega=2.95$. Both α^* and Re_t are calculated using Eq. (14). For the high Reynolds number version of the turbulence model $\alpha=\alpha_\infty=1$.

The dissipation of k is given by

$$Y_k = \rho \beta^* f_{\beta^*} k\omega \tag{17}$$

where

$$f_{\beta^*} = \begin{cases} 1 & \chi_k \le 0 \\ \dfrac{1+680\chi_k^2}{1+400\chi_k^2} & \chi_k > 0 \end{cases} \tag{18}$$

where

$$\chi_k \equiv \frac{1}{\omega^3} \frac{\partial k}{\partial x_j} \frac{\partial \omega}{\partial x_j} \tag{19}$$

and

$$\beta^* = \beta^*_i [1 + \zeta^* F(M_t)] \tag{20}$$

$$\beta^*_i = \beta^*_\infty \left[\frac{4/15 + (\mathrm{Re}_t/R_\beta)^4}{1 + (\mathrm{Re}_t/R_\beta)^4} \right] \tag{21}$$

with $\zeta=1.5$, $R_\beta=8$, $\beta^*_\infty=0.09$, and Re_t is defined above.

The dissipation of ω is governed by a similar equation

$$Y_\omega = \rho \beta_i f_\beta \omega^2 \tag{22}$$

where

$$f_\beta = \frac{1+70\chi_\omega}{1+80\chi_\omega} \tag{23}$$

$$\chi_\omega = \left| \frac{\Omega_{ij}\Omega_{jk}S_{ki}}{(\beta^*_\infty a)^3} \right| \tag{24}$$

$$\Omega_{ij} = \frac{1}{2} \left(\frac{\partial u_i}{\partial x_j} - \frac{\partial u_j}{\partial x_i} \right) \tag{25}$$

3 Validation Study

3.1 Setup. The first task undertaken for evaluating the suitability of turbulence models within FLUENT was to extend previously published work by Varghese and Frankel [12] based on the experimental models of Ahmed and Giddens [11]. The computational model was set up for a 75% reduction in area and was created within GAMBIT, the pre-processing package for FLUENT, using information taken from the Ahmed and Giddens paper. The diameter of the stenosed vessel, D, was 0.0508 m. The inflow and outflow boundaries were created $97D$ upstream and $13D$ downstream of the start and end of the stenosis curve, respectively, so as to closely resemble the experimental setup. Thus, the wave form in Fig. 1, taken from Varghese and Frankel and created as a user defined function (UDF) within FLUENT, was applied as a flat velocity profile at the inflow boundary. This is in contrast to recent work by Ryval et al. [7], who recommended fully developed inlet flow profiles when simulating a shortened section of the experimental domain. Each flow simulation modeled three complete pulses of the inflow velocity wave form with the data being extracted from the third pulse. Snapshots of the simulations were taken at each of the time steps highlighted in Fig. 1 and these mirror the reporting times from both reference papers.

The incompressible Reynolds averaged Navier Stokes (RANS) equations were solved using the segregated axi-symmetric solver together with the two equation turbulence models. Whereas the $k-\omega$ model is formulated to integrate through the boundary layer, the $k-\epsilon$ RNG turbulence model mimics this behavior by using an enhanced wall function configuration which defines the law of the

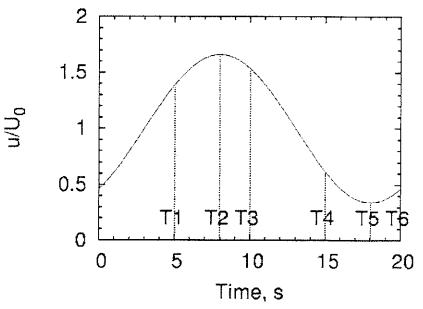

Fig. 1 Inflow velocity profile

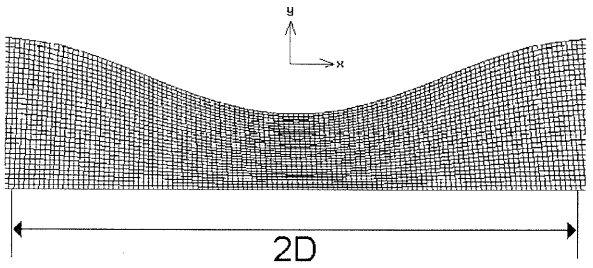

Fig. 2 Computational model and mesh structure

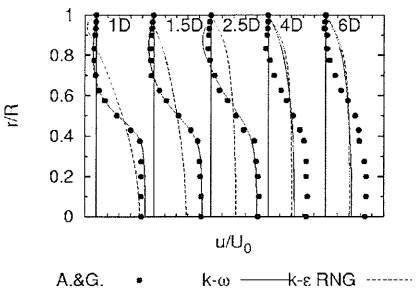

Fig. 3 Axial velocity profile comparisons at locations distal to the stenosis at T2. The range for each profile is between 0 and 5 u/U_o.

wall as a single equation that is valid for the entire wall region.

The equations were solved using second-order upwind discretization methods and the pressure implicit splitting of operators (PISO) algorithm. The simulations utilized a second-order implicit time stepping scheme with a time step of 0.002 s. The computational mesh consisted of 125,250 quadrilateral cells mapped throughout the domain. A finer computational mesh was created with approximately 820,000 cells to assess the accuracy of the 125k mesh. These mesh configurations are comparable to the 60 and 120 point meshes in Varghese and Frankel[12]. The values for the time step were based on information supplied by Varghese and Frankel. The constricted section of the computational model and mesh structure are displayed in Fig. 2. Blood was modeled as an incompressible Newtonian liquid with density $\rho=1000\ \mathrm{kg\,m^{-3}}$ and dynamic viscosity $\mu=0.0036014\ \mathrm{kg\,m^{-1}s^{-1}}$. The mean velocity, U_0, of the inflow profile used for the simulations was $0.04254\ \mathrm{m\,s^{-1}}$ and the mean Reynolds number for the simulations was 600. The peak and minimum Reynolds numbers were 996 and 204, respectively. The Womersley number, α, was approximately 7.5.

The turbulence intensity, I, and turbulence length scale, l, were specified at the inflow boundary condition using

$$I = 0.16(\mathrm{Re}_{D_H})^{-1/8} \tag{26}$$

$$l = 0.07L = 0.07D \tag{27}$$

with

$$\mathrm{Re}_{D_H} = \frac{\rho U_o D}{\mu} \tag{28}$$

where D was the diameter of the tube. The values used for the validation study as recommended by FLUENT [13] are 7.2% for the turbulence intensity and 0.003556 m for the turbulence length scale. Further investigations looking at the influence of the inflow boundary conditions on the validation geometry are discussed in Sec. 3.2

3.2 Results and Discussion

3.2.1 Velocity Profile Comparisons. Data for the velocity profiles from the snapshot taken at T2 are compared to Ahmed and Giddens experimental results. The data for both turbulence models are plotted in Fig. 3 with each axial location offset by five units on the x axis. The $k-\omega$ turbulence model shows good agreement for both mesh densities against the experimental data from Ahmed and Giddens for the data recorded at $1D$, $1.5D$, and $2.5D$ downstream of the stenosis. The area and values of reversed flow for the data at $1D$ and $1.5D$ virtually match the experimental data. The $k-\omega$ simulation also provides a better fit for the increase in the core flow velocity nearer to the center of the tube. A small difference in the recirculation area at $2.5D$ can be observed between the two computational meshes for the $k-\omega$ models. The $k-\epsilon$ RNG turbulence model predicts a smaller region of reversed flow at $1D$ and no reversed flow at the other locations. The core flow velocity also reduces faster than the $k-\omega$ model and transforms into a flatter uniform velocity profile throughout the downstream section of the tube. At $4D$ and $6D$ the data from the $k-\omega$ and the $k-\epsilon$ RNG models collapse onto each other. At both of these regions neither turbulence model matches the characteristics of the experimental data.

There are some similarities with the data from the Varghese and Frankel simulations. The $k-\omega$ model produces a higher velocity than the three variants of the $k-\epsilon$ model they tested and the $k-\omega$ model corresponds to the results from the experimental data closer than their $k-\epsilon$ runs. Surprisingly neither of the turbulence models tested in the Varghese and Frankel paper show any areas of reversed flow downstream of the stenosis. This is one area where their data fail to capture the trend of the experimental data.

3.2.2 Influence of Inflow Boundary Conditions. The effects of changing the turbulence intensity at the inflow boundary condition were investigated for each of the turbulence models. Four different values of turbulence intensity were analyzed (10%, 7.2%, 3.6%, and 0%) and results for the axial velocity, turbulence intensity, and turbulent viscosity assessed at $1D$, $1.5D$, $2.5D$, $4D$ and $6D$ downstream of the stenosis throat. The turbulence intensity and turbulent viscosity for the $k-\epsilon$ RNG model are shown at T2 in Figs. 4 and 5, respectively. Each location is offset by five units on the x axis. The downstream profiles of intensity and turbulent viscosity are invariant with changes in the boundary conditions. Thus, the velocity profiles are similarly unaffected as shown in Fig. 6. In contrast, the velocity profiles for the $k-\omega$ model depicted in Fig. 7 show a small but noticeable variation, resulting from the differences in intensity and turbulent viscosity shown in Figs. 8 and 9. These results demonstrate that the transitional $k-\omega$ model responds sensibly to variations in levels of inlet turbulence. At relatively high values ($I>7.2\%$), the turbulent viscosity is sufficiently high enough to influence the transport of momentum. When inlet intensity approaches zero, the flow remains laminar as there is no increase in the effective viscosity.

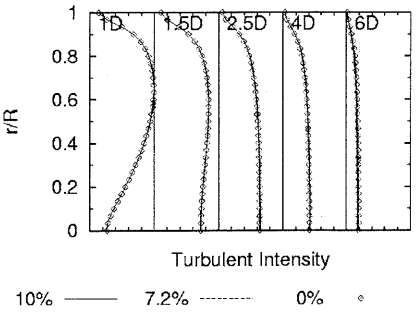

Fig. 4 Turbulence intensity at T2, $k-\epsilon$ RNG model. The range for each profile is between 0% and 100%.

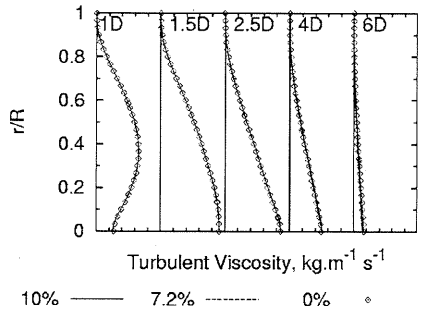

Fig. 5 Turbulent viscosity at T2, $k-\epsilon$ RNG model. The range for each profile is between 0 Ka m^{-1} s^{-1} and 0.2 kg m^{-1} s^{-1}.

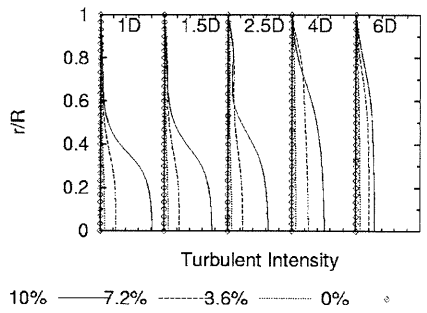

Fig. 8 Turbulence intensity at T2, $k-\omega$ model. The range for each profile is between 0% and 40%.

4 Computational Model of the Carotid Artery Bifurcation

The geometry model of the carotid artery bifurcation was constructed within the CATIA V5 CAD package (Dassault Systemes). The design of the carotid artery bifurcation was based on the tuning fork shape as proposed by Smith et al. [14] and Ding et al. [15]. The values for the parameters controlling the shape were taken from data in Bharadvaj et al. [16] and Ding et al. [15]. The three-dimensional model was created by adding circular sectional profiles to a two-dimensional longitudinal section. Shape control, especially for the sinus bulb, was achieved by using Bezier curves to define the curves in the two-dimensional section. Further details on the definition and construction of the CAD model can be found in Bressloff et al. [17]. In contrast to ongoing work that is investigating the effect of varying a number of shape parameters simultaneously, here we simply vary the shape of the entry to the sinus bulb so as to mimic the effect of different degrees of stenosis. Thus, it is possible to explore the interaction between turbulent flow simulation and the level of area constriction, while maintaining a constant shape elsewhere.

Three levels of stenosis are simulated with respect to sinus bulb area reduction: mild (25%), moderate (50%), and severe (75%). The computational model with the severe stenosis configuration is displayed in Fig. 10.

5 3D Flow Studies

5.1 Setup. The diameter for the common carotid artery was set at 8 mm for each of the stenosed bifurcation models. The branch angles for the internal and external carotid artery branches were constant at 25.4 deg and 25.1 deg, respectively. A realistic mean inflow pulse (cf. Fig. 11) for the common carotid artery was taken from Holdsworth et al. [18] and the details of the Fourier series representation were kindly supplied by D. A. Steinman. The Fourier series and Fourier coefficients (numbered from 0) are given by Eq. (29) and Table 3

$$\text{Velocity} = \frac{1}{16\pi}\left\{ a_0 + \sum_{n=1}^{13}\left[a_n \cos\left(\frac{2n\pi t}{0.917}\right) + b_n \sin\left(\frac{2n\pi t}{0.917}\right)\right]\right\} \tag{29}$$

The pulse was modeled by applying a flat velocity profile at the inflow boundary, and only two complete pulses were required before the simulation became invariant between pulses. The mean Reynolds number for the inflow pulse for these simulations is approximately 277. The peak and minimum Reynolds numbers for the wave form are 1104 and 17, respectively. Blood is modeled as an incompressible Newtonian liquid with the following values: $\rho = 1035$ kg m^{-3} and $\mu = 0.0035$ kg m^{-1} s^{-1}. The flow splits between the ICA and ECA (external carotid artery) were defined as

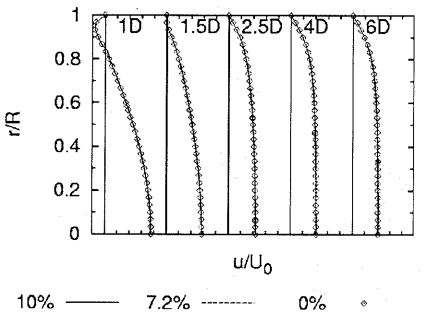

Fig. 6 Velocity profiles at T2, $k-\epsilon$ RNG model. The range for each profile is between 0 u/U_0 and 5 u/U_0.

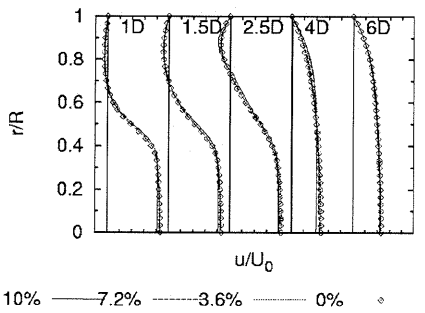

Fig. 7 Velocity profiles at T2, $k-\omega$ model. The range for each profile is between 0 u/U_0 and 5 u/U_0.

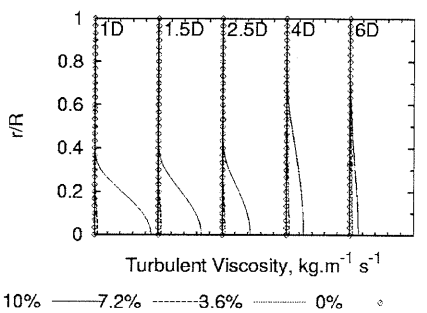

Fig. 9 Turbulent viscosity at T2, $k-\omega$ model. The range for each profile is between 0 kg m^{-1} s^{-1} and 0.08 kg m^{-1} s^{-1}.

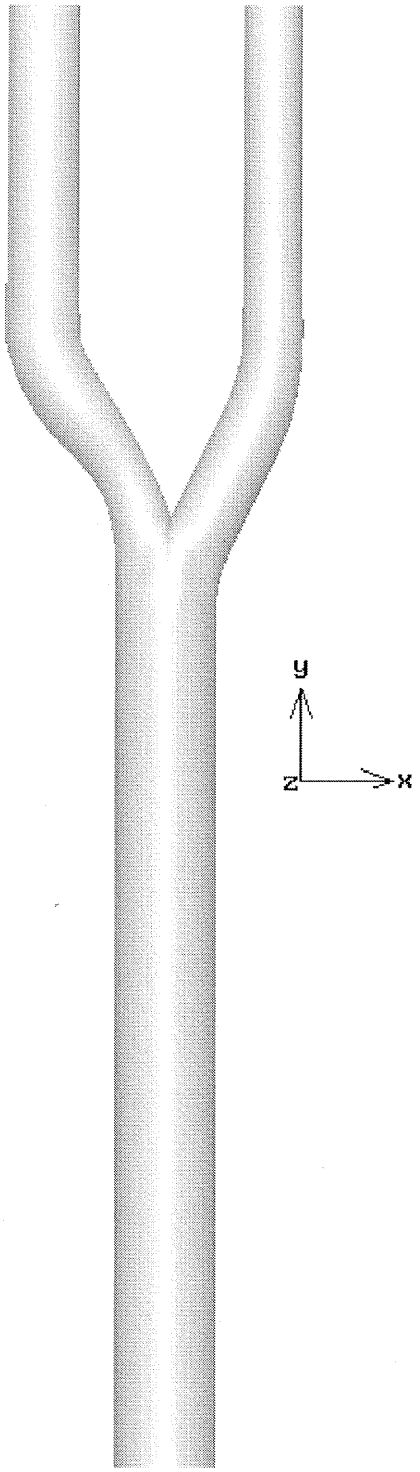

Fig. 10 Computational model—severe stenosis configuration

70:30. The same solution scheme was used as for the validation study. However, due to the earlier findings, only the $k-\omega$ model was used.

5.2 Mesh Dependence. A mesh dependence study was undertaken on the mild, moderate, and severe stenosis configurations.

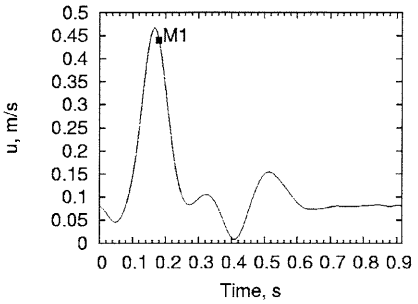

Fig. 11 Pulse waveform for the common carotid artery

Figure 11 depicts point M1 where the velocity profiles through and downstream of the ICA sinus bulb were analyzed. The locations for the velocity profiles at the entry, middle, and exit of the sinus bulb on the center plane of the model are shown in Fig. 12, and three further locations downstream of the sinus bulb were also extracted. Previous work for a baseline unstenosed carotid artery bifurcation model in 2D and 3D steady flow configurations

Table 3 Fourier coefficients for the inflow velocity wave form

n	a_n	b_n
0	6.000	0.000
1	1.076	2.989
2	−2.315	3.071
3	−2.705	−1.979
4	−0.639	−1.583
5	1.775	−1.903
6	1.168	1.065
7	−0.202	0.578
8	−0.267	0.152
9	−0.152	−0.202
10	0.142	−0.133
11	0.118	0.022
12	0.056	0.050
13	0.010	0.072

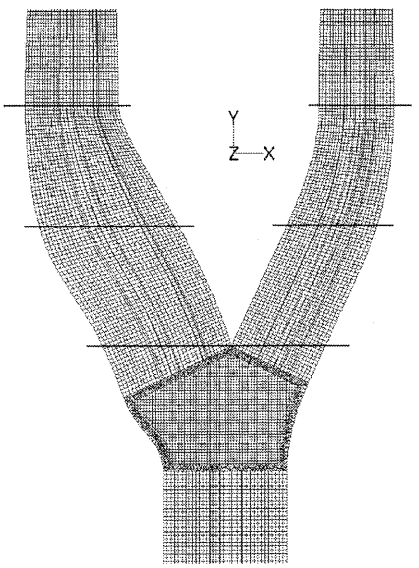

Fig. 12 Computational mesh (z=0) for mild stenosis model. The three locations in the sinus bulb used to analyze the velocity profiles are displayed.

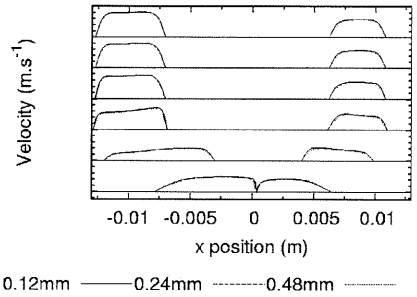

Fig. 13 Mild stenosis streamwise velocity profiles at M1. The range for each profile is between 0 m s^{-1} and 1 m s^{-1}.

yielded mesh and time independence with a 0.48 mm mesh interval and 10^{-4} for the time step. Mesh dependence in the present study compared three mesh densities using fixed meshing intervals of 0.12 mm (4.1 million cells), 0.24 mm (680,000 cells), and 0.48 mm (110,000 cells), and a time step of 10^{-4}. Approximate computational times to simulate one complete inflow pulse using an AMD 2.2 GHz Opteron are ~6 h for the 0.48 mm mesh and 4 days for the 0.24 mm mesh. The 0.12 configuration was undertaken using FLUENT in parallel and used eight AMD 2.2 GHz Opterons each with 2GB RAM and the runtime was approximately 2 days. The model is meshed using structured hexahedral cells in the common carotid, internal carotid, and external carotid tubes. The bifurcation region is meshed using the hexcore scheme available in GAMBIT. Figures 13–15 display, respectively, the mild, moderate, and severe stenosis velocity profiles for each of the mesh densities. The data for the entry into the sinus bulb is at the bottom of each figure with subsequent locations offset by one additional unit on the y axis. In nearly every case, very close agreement is obtained between all meshes with only a few minor deviations for the coarsest mesh. Although not shown here, identical results were also obtained for a time step of 10^{-5} s.

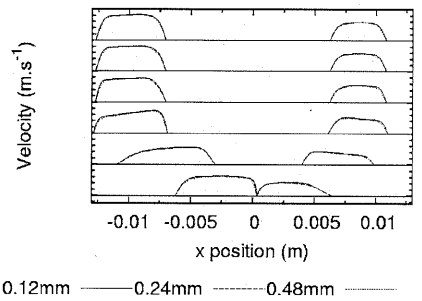

Fig. 14 Moderate stenosis streamwise velocity profiles at M1. The range for each profile is between 0 m s^{-1} and 1 m s^{-1}.

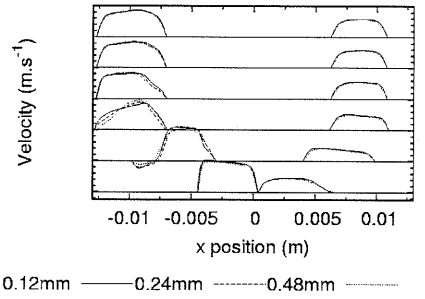

Fig. 15 Severe stenosis streamwise velocity profiles at M1. The range for each profile is between 0 m s^{-1} and 1 m s^{-1}.

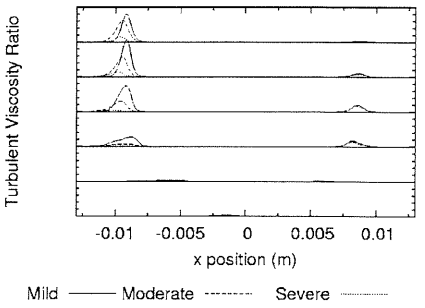

Fig. 16 Turbulent viscosity ratio at M1. The range for each profile is between 0 and 0.2.

5.3 Results and Discussion

5.3.1 Turbulence Parameters Comparison. Comparison with recent experimental data[19] confirms that turbulence levels are generally low in the simulations performed here. While recognizing that there are notable differences in boundary conditions and that the data in Ref. [19] is for concentric stenosis, the experimentally measured peak turbulence intensity is nearly an order of magnitude higher than that in the equivalent eccentric stenosis here.

The turbulent viscosity ratio for all of the stenosis configurations using the finest mesh is plotted in Fig. 16 for each location. The mild stenosis configuration displays the largest turbulent viscosity ratio in the ICA and this can be explained by considering the other turbulence parameters. The kinetic energy, k, is also high for the mild stenosis configuration with the lowest values recorded for the severe stenosis (cf. Fig. 17). The turbulent viscosity, μ_t, is calculated using Eq. (13) and uses both k and ω, the specific dissipation rate. For each of the stenosis configurations considered the specific dissipation rate is very similar with the severe stenosis producing slightly higher rates in the sinus bulb region. Thus, in the mild stenosis, since the turbulent kinetic energy is significantly larger, the turbulent viscosity is also higher than in the other stenoses.

In the ECA branch of the bifurcation, the values for the turbulent viscosity ratio, kinetic energy, and specific dissipation rate are identical for each of the stenosis configurations.

5.3.2 Flow Visualization. According to the NASCET method of stenosis classification, the severe stenosis equates to a 25% reduction. Figure 18 depicts velocity profiles on planes in this model similar to those shown in Steinmann et al. [20] for a 30% eccentric stenosis at a similar time in the pulse. In [20], simulations are treated as laminar, and their outflow ratios between the ICA and ECA are different from those used here. Nonetheless, the peak velocity of 1.1 m s^{-1} corresponds well with their peak velocity value and the characteristic jet like flow against the inner ICA

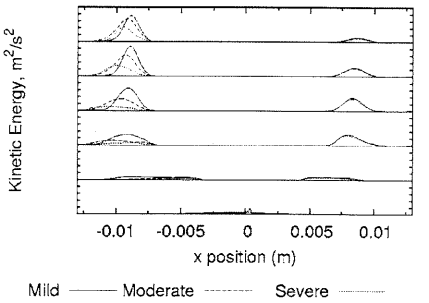

Fig. 17 Turbulent kinetic energy at M1. The range for each profile is between 0 m s^{-1} and 0.0005 m^2/s^2.

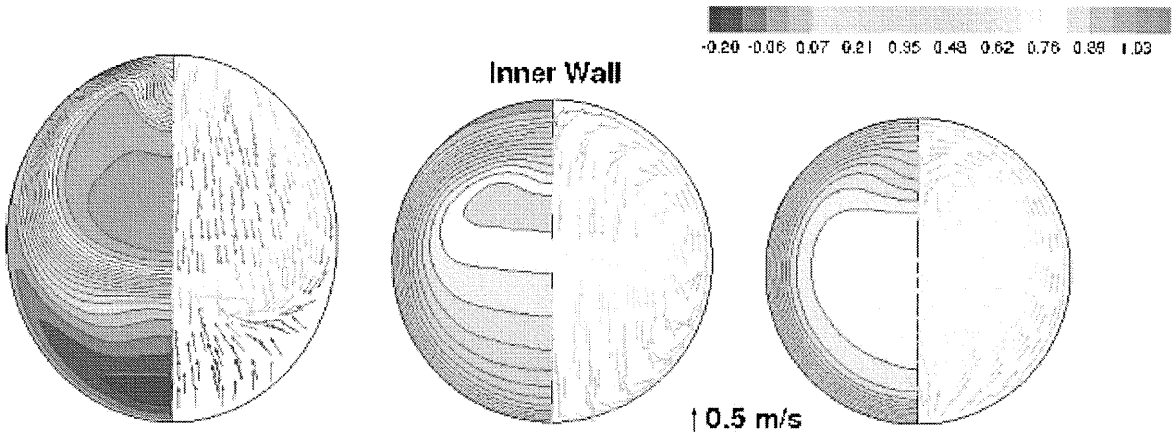

Fig. 18 *y* **velocity component flow patterns for M1 (*t*=0.18 s) at *y*=1D, 2D, and 3D**

wall can be seen in the first slice and the region of slower flow is also present on the ICA outer wall. The in-plane velocity vectors are similar for the first two locations with the third location displaying stronger secondary flow features, with small Dean-type vortices being present close to the ICA inner wall.

The negative *y* component of wall shear stress was analyzed for each of the stenosis configurations and the contour plots are displayed in Fig. 19. The mild stenosis case displays no negative wall shear stress after the stenosis but there is a small recirculation zone upstream of the stenosis. The moderate stenosis configuration displays a region of negative wall shear stress distal to the stenosis with the peak value approximately −5 Pa. The severe

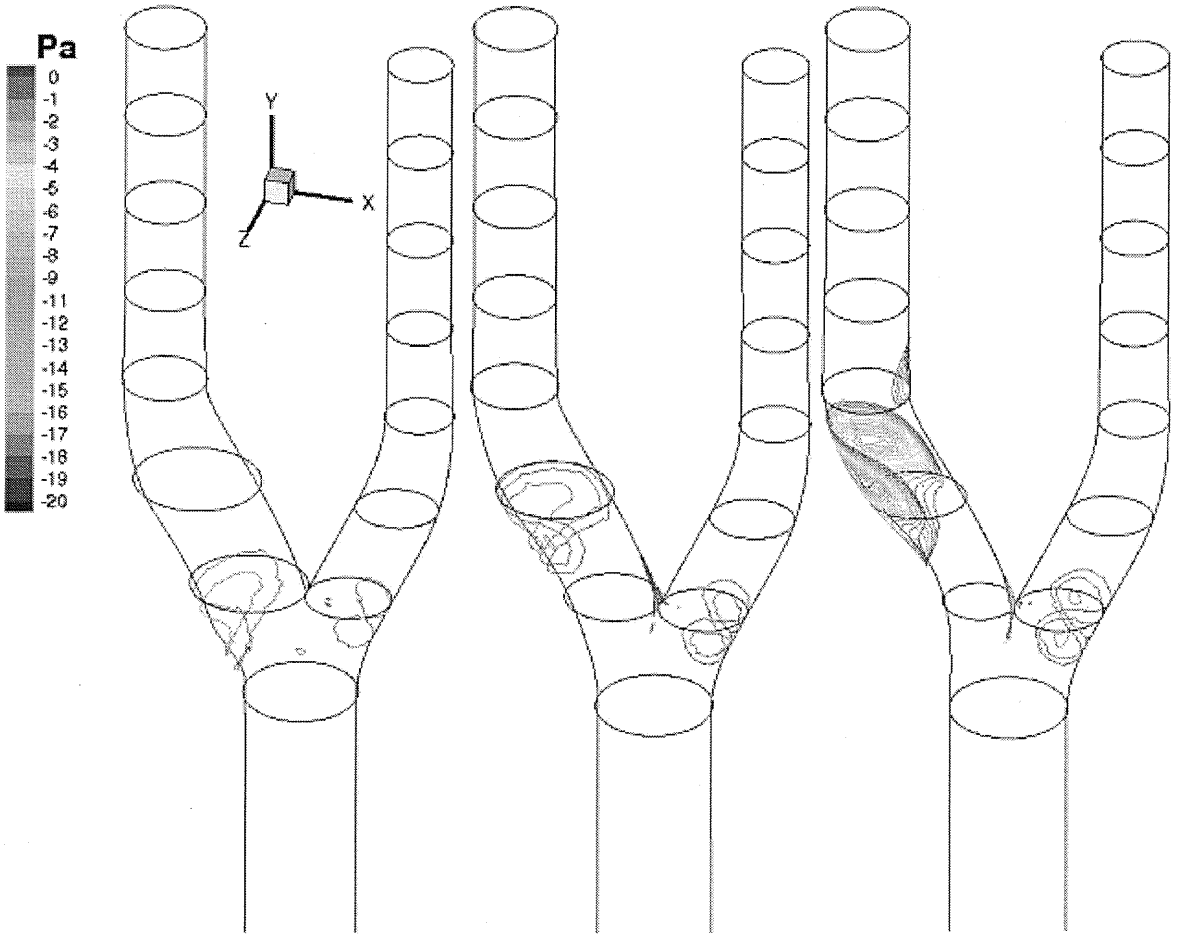

Fig. 19 Negative wall shear stress (streamwise component) at M1 (*t*=0.18 s)

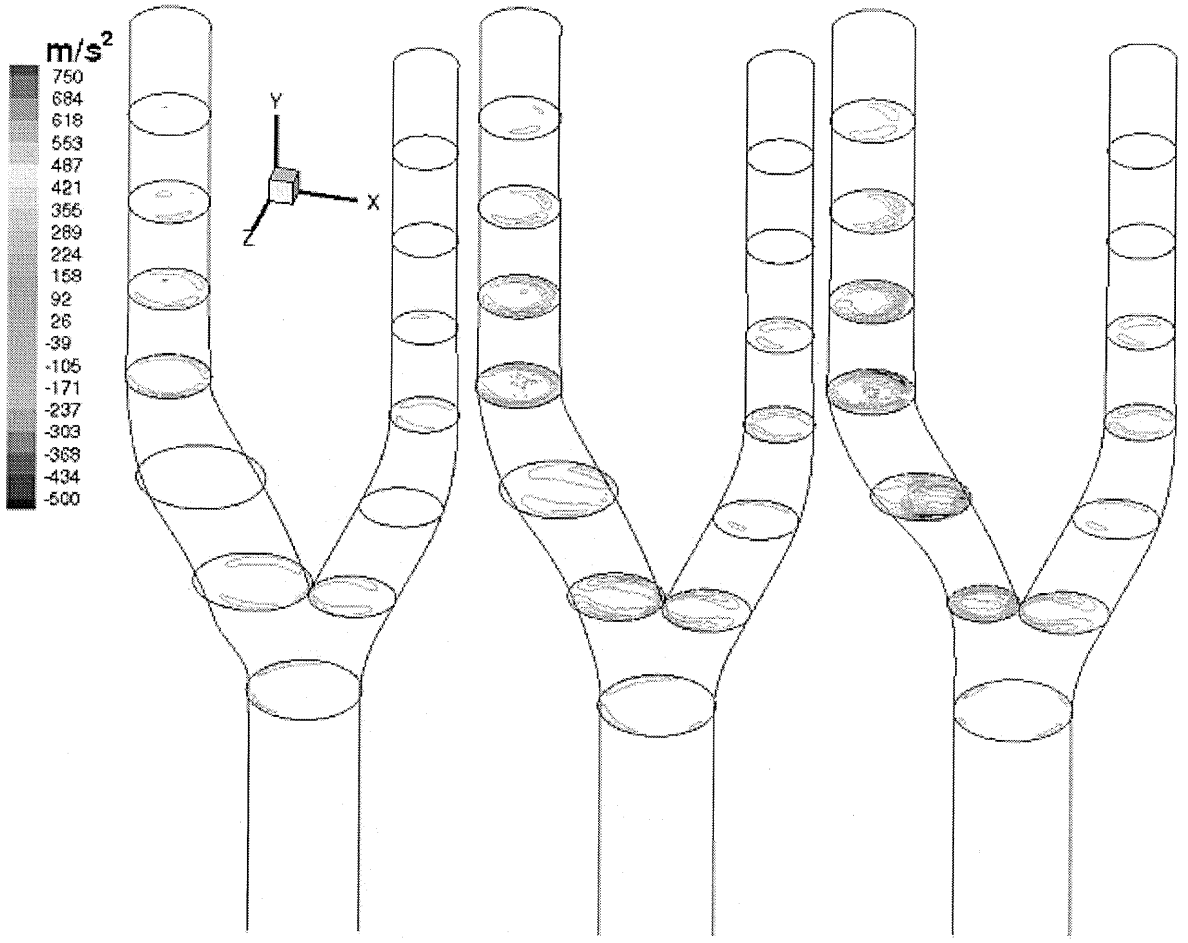

Fig. 20 Helicity profiles at M1 (t=0.18 s)

configuration displays a larger region of negative wall shear stress distal to the stenosis with a peak value of −20 Pa. Also, a smaller region is located on the inner internal carotid wall downstream of the sinus bulb. This region is generated by the increased velocity of the flow through the sinus bulb being unable to enter the outflow section of the ICA without separating. Each of the stenosis configurations display small regions of low negative wall shear stress in the ECA branch with the size and magnitude increasing with stenosis severity.

Further insight into the effect of the degree of stenosis is provided by the helicity

$$\text{Helicity} = (\nabla \times \mathbf{U}) \cdot \mathbf{U} \tag{30}$$

This represents the alignment of the vorticity vector with the fluid stream. In other words, the helicity describes the speed at which vorticity is convected downstream. Contour plots in the $x-z$ plane were created at each of the locations used to analyze the velocity profiles above (cf., Fig. 20).

Each of the configurations displays regions of helicity with the magnitude and size of the regions increasing with stenosis severity. For the severe stenosis configuration the helicity at each of the locations in the sinus bulb region is much stronger than the mild and moderate cases. This stronger helicity persists downstream in the internal carotid but returns to similar values at the last location. The helicity profiles in the external carotid branch are very similar for each of the stenosis configurations, suggesting that some helicity is being generated by the tuning fork representation of the carotid artery bifurcation.

The flow variables were also analyzed at a point further along the inflow pulse at t=0.25 s where the flow is decelerating. The main observations to make concern the helicity which, as shown in Fig. 21, is still relatively strong in the severe stenosis, but has diminished in the mild and moderate stenoses.

6 Conclusions

The flow within a constricted geometry has been modeled using transitional $k-\omega$ and $k-\epsilon$ RNG turbulence models. An axisymmetric, full length representation is constructed of the test rig from which experimental data are compared. The transitional $k-\omega$ model provides better agreement with experimental results through the recirculation region but shows similar discrepancies to the $k-\epsilon$ model further downstream. The sensitivity of both models to variations in turbulence quantities at the inflow is also investigated. The $k-\epsilon$ model shows no sensitivity in velocity, turbulence intensity, or viscosity ratio to changes in inlet turbulence intensity, whereas the $k-\omega$ model produces significant differences in the downstream turbulence quantities leading to noticeable variations in the velocity profiles.

Following this preliminary work, the $k-\omega$ model was then applied to simulations within a computational model of a mean carotid artery bifurcation. Using a CAD definition of this shape, three degrees of stenosis were generated while keeping the overall shape fixed. Although the severe stenosis produces larger, stronger

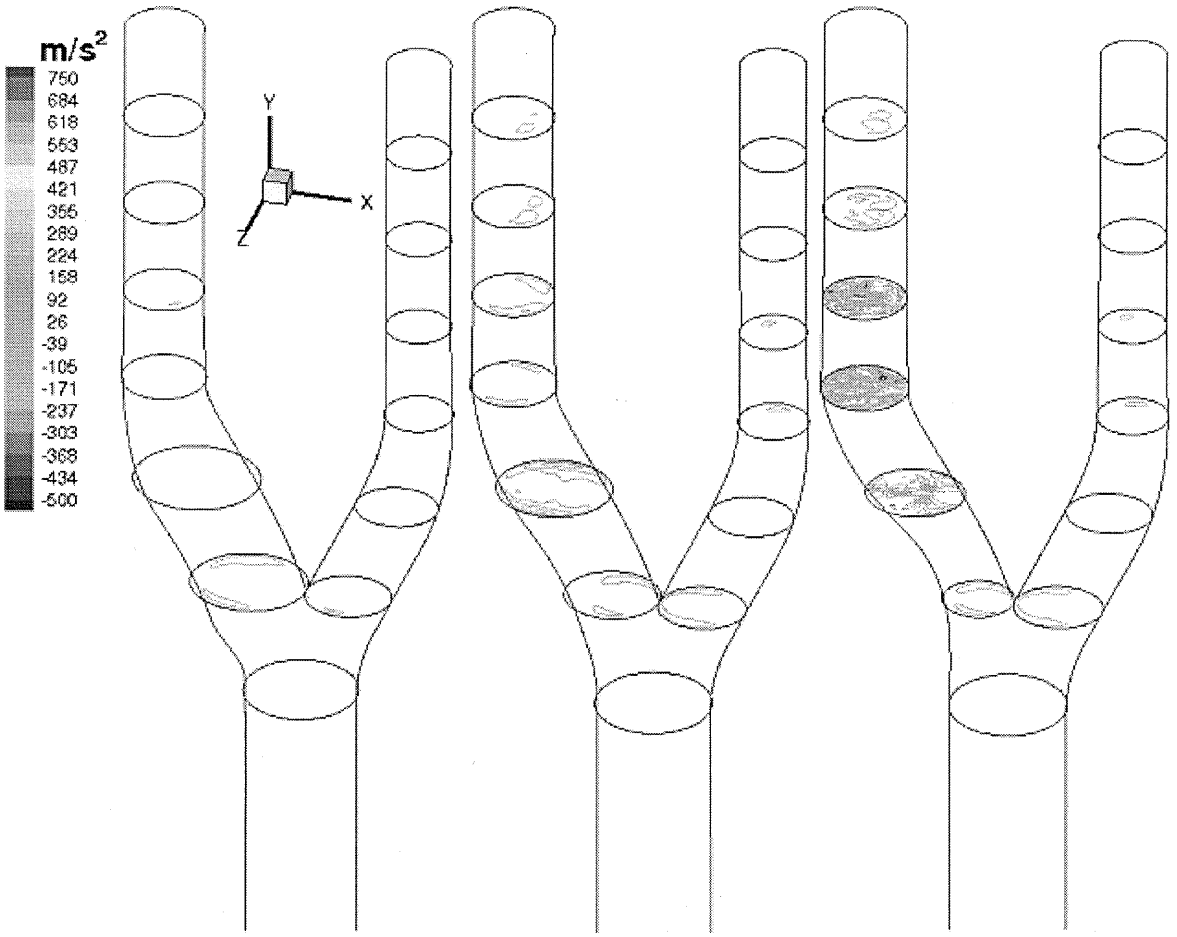

Fig. 21 Helicity profiles at t=0.25 s

regions of recirculation and higher values of vorticity and helicity than the mild and moderate stenoses, the presence of turbulence (as predicted by this eddy viscosity model) produces an unexpected effect. Due to the dependence of the turbulent viscosity, μ_t on the turbulent kinetic energy, k, and the specific dissipation rate, ω, it would seem that high values of both k and ω in the severe stenosis model lead to low values of μ_t relative to the mild stenosis. Consequently, turbulence has a relatively weaker effect on the flow field through the severe stenosis, as measured by the smaller impact on the effective viscosity, $\mu_{\text{eff}}=\mu+\mu_t$. However, turbulence levels are relatively low in all models when compared to experimental data from similar degrees of stenosis in concentrically modified shapes. Thus, direct validation of pulsatile RANS models is still required before determining their suitability for highly stenotic bifurcation simulations exposed to a wide range of Reynolds numbers encompassing transition. Ultimately, alternative approaches may be required (e.g., large eddy simulation) to accurately simulate this complex flow regime. With this in mind, the parametric geometry model developed in this preliminary study is now being extended so that it can be used to capture patient specific geometry, the flow through which will be used to validate commonly used turbulence models and to test the suitability of alternative approaches.

Nomenclature

D = diameter of the artery (m)
R = radius of the artery (m)
Re = reynolds number, $\rho UD/\mu$
U_0 = mean velocity for the inflow profile (m s^{-1})
$\bar{Z}$ = nondimensional axial distance, Z/D, where Z is measured from the throat of the stenosis
ρ = density of the fluid (kg m^{-3})
μ = dynamic viscosity of the fluid (kg m^{-1} s^{-1})
μ_t = turbulent dynamic viscosity of the fluid (kg m^{-1} s^{-1})
μ_{eff} = effective dynamic viscosity ($\mu+\mu_t$)

References

[1] Beaglehole, R., Irwin, A., and Prentice, T., 2003, "Facts and Figures: The World Health Report 2003—Shaping the Future," World Health Organization, Tech. Rep.
[2] Ku, D., 1997, "Blood Flow in Arteries," Annu. Rev. Fluid Mech., **29**, pp. 399–434.
[3] Berger, S., and Jou, L., 2000, "Flows in Stenotic Vessels," Annu. Rev. Fluid Mech., **32**, pp. 347–382.
[4] Schulz, U. G., and Rothwell, P. M., 2001, "Major Variation in Carotid Artery Bifurcation Anatomy —A Possible Risk Factor for Plaque Development?," Stroke, **32**, pp. 2522–2529.
[5] Ghalichi, F., Deng, X., De Champlain, A., Douville, Y., King, M., and Guidoin, R., 1998, "Low Reynolds Number Turbulence Modeling of Blood Flow in Arterial Stenoses," Biorheology, **35**, pp. 281–294.
[6] Stroud, J., Berger, S., and Saloner, D., 2002, "Numerical Analysis of Flow Through a Severely Stenotic Carotid Artery Bifurcation," ASME J. Biomech. Eng., **124**, pp. 9–20.
[7] Ryval, J., Straatman, A., and Steinman, D., 2004, "Two-Equation Turbulence Modeling of Pulsatile Flow in a Stenosed Tube," ASME J. Biomech. Eng., **126**, pp. 625–635.

[8] Younis, B., and Berger, S., 2004, "A Turbulence Model for Pulsatile Arterial Flows," ASME J. Biomech. Eng., **126**, pp. 578–584.
[9] Mittal, R., Simmons, S., and Udaykumar, H., 2001, "Application of Large-Eddy Simulation to the Study of Pulsatile Flow in a Modeled Arterial Stenosis," ASME J. Biomech. Eng., **123**, pp. 325–332.
[10] Mittal, R., Simmons, S., and Najjar, F., 2003, "Numerical Study of Pulsatile Flow in a Constricted Channel," J. Fluid Mech., **485**, pp. 337–378.
[11] Ahmed, S., and Giddens, D., 1984, "Pulsatile Poststenotic Flow Studies with Laser Doppler Anemometry," J. Biomech., **17**, pp. 695–705.
[12] Varghese, S., and Frankel, S., 2003, "Numerical Modeling of Pulsatile Turbulent Flow in a Stenosed Tube," ASME J. Biomech. Eng., **126**, pp. 625–635.
[13] Fluent Inc., 2003, *The Fluent 6.1 Users Manual*, Lebanon, NH.
[14] Smith, R., Rutt, B., Fox, A., and Rankin, R., 1996, "Geometric Characterization of Stenosed Human Carotid Arteries," Radiology, **3**, pp. 898–911.
[15] Ding, Z., Wang, K., Li, J., and Cong, X., 2001, "Flow Field and Oscillatory Shear Stress in a Tuning-Fork-Shaped Model of the Average Human Carotid Bifurcation," J. Biomech., **34**, pp. 1555–1562.
[16] Bharadvaj, B., Mabon, R., and Giddens, D., 1982, "Steady Flow in a Model of a Human Carotid Bifurcation. Part 1—Flow Visualization," J. Biomech., **15**, pp. 349–362.
[17] Bressloff, N., Forrester, A., Banks, J., and Kolachalama, V., 2004, "Shape Optimization of the Carotid Artery Bifurcation," *Proceedings 5th ASMO UK/ ISSMO Conference on Engineering Design Optimisation*, Stratford-upon-Avon, UK, July 12–13.
[18] Holdsworth, D., Norley, C., Frayne, R., Steinman, D., and Rutt, B., 1999, "Characterization of Common Carotid Artery Blood-Flow Waveforms in Normal Human Subjects," Physiol. Meas, **20**, pp. 219–240.
[19] Poepping, T. L., Nikolov, H. N., Rankin, R. N., Lee, M., and Holdsworth, D. W., 2002, "An in Vitro System for Doppler Ultrasound Flow Studies in the Stenosed Carotid Artery Bifurcation," Ultrasound Med. Biol., **28**(4), pp. 495–506.
[20] Steinman, D., Poepping, T., Tambasco, M., Rankin, R., and Holdsworth, D., 2000, "Flow Patterns at the Stenosed Carotid Bifurcation: Effect of Concentric Versus Eccentric Stenosis," Ann. Biomed. Eng., **28**, pp. 415–423.